Sustainable Energy & Fuels

PAPER

View Article Online
View Journal | View Issue

Cite this: *Sustainable Energy Fuels*, 2018, **2**, 1986

Nickel-iron catalysts for electrochemical water oxidation – redox synergism investigated by *in situ* X-ray spectroscopy with millisecond time resolution†

Diego González-Flores,[abcd] Katharina Klingan,[a] Petko Chernev,[a] Stefan Loos,[a] Mohammad Reza Mohammadi,[a] Chiara Pasquini,[a] Paul Kubella,[a] Ivelina Zaharieva,[a] Rodney D. L. Smith[a] and Holger Dau*[a]

In future technological systems for chemical storage of renewable energy and production of non-fossil fuels, NiFe oxyhydroxides are prime candidates for efficient alkaline water oxidation (oxygen evolution reaction, OER). The synergistic effect of Ni and Fe is well documented but still insufficiently understood. Fluorescence-detected X-ray absorption spectroscopy at the K-edges of Ni and Fe provided structural information on the non-catalytic (reduced) and catalytic (oxidized) state of the NiFe catalyst. Time-resolved detection of X-ray signals during (i) cyclic voltammetry and (ii) in response to potential steps revealed that the Ni(2+)/Ni(3+) redox transition is directly coupled to modification of the Fe ligand environment. We propose that the lattice-geometry modification of the Ni(Fe) oxyhydroxide that results from Ni oxidation enforces changes in the ligand environment of the Fe ions. The Fe sites do not undergo a distinctive redox transition, but are "enslaved" by the oxidation state changes of the Ni ions.

Received 7th March 2018
Accepted 9th April 2018

DOI: 10.1039/c8se00114f

rsc.li/sustainable-energy

1. Introduction

One of the major goals in research on efficient water splitting for production of non-fossil fuels is the rational design of the catalyst for the anodic water oxidation process, the oxygen evolution reaction (OER). Of special interest are catalyst materials based on earth-abundant, non-precious metals. Accomplishing this goal requires a better understanding of the catalyst function, especially regarding the determinants for high catalytic activity. From this perspective, NiFe based catalysts are of special interest due to their high activity at low overpotentials in alkaline conditions, at levels comparable to the most efficient noble metal based catalyst.[1–6] The high catalytic activity of NiFe oxyhydroxides is well known for more than 60 years. Early discovery reports can be traced back to the 1950's.[7] However these materials had not been studied in more depth until the 1980's when the interest in water splitting was rising.[8,9] With the steadily increasing interest in water splitting, many recent studies have focused on the catalytic mechanism of NiFe oxide (or hydroxide) catalysts.[10–12] Understanding the function of the catalyst requires insights in structure–function relations, including dynamic restructuring induced by changes of the electrochemical potential, and identification of the catalytically active site.

Formation of the $NiFe_2O_4$ inverse spinel has been associated with the catalytic activity.[13] However, Raman spectroscopic evidence suggested this is not the main active phase.[14] Most of the recent investigations point towards a Ni(Fe) oxyhydroxide phase that likely is decisive for catalytic activity.[10,15] For a long time it has been believed that this active phase consists of β-Ni(Fe)OOH.[16] However, more recent reports indicate the γ-Ni(Fe)OOH as the phase responsible of the catalytic activity.[10,15] Bell and coworkers have suggested that during operation the iron-containing α-$Ni(OH)_2$ is transformed into γ-Ni(Fe)OOH.[10] They found that Ni increases its oxidation state to +3.6 and iron remains in its +3 oxidation state, but with unusually short Fe–O distances; and they proposed that the short distances in the iron result from the constraints imposed by the γ-NiOOH structure.

The effect of Fe in enhancing the catalytic activity is undeniable.[9,17–21] However, the reason for this improvement is not clear. It has been suggested that it is related to an increment of the conductivity of the film by the incorporation of Fe, but further factors are likely involved.[17] Most of the debate is now focusing on the question whether the active site corresponds to Fe^{4+}, Fe^{3+} or Ni^{4+} sites.[10,12,22,23]

[a]*Department of Physics, Freie Universität Berlin, Arnimallee 14, 14195 Berlin, Germany. E-mail: holger.dau@fu-berlin.de*

[b]*Centro de Electroquímica y Energía Química (CELEQ), Universidad de Costa Rica, 11501 2060, San José, Costa Rica*

[c]*Centro de Investigación en Ciencia e Ingeniería de Materiales (CICIMA), Universidad de Costa Rica, 11501 2060, San José, Costa Rica*

[d]*Escuela de Química, Universidad de Costa Rica, 11501 2060, San José, Costa Rica*

† Electronic supplementary information (ESI) available. See DOI: 10.1039/c8se00114f

Some groups have suggested the formation of Fe^{4+} with Fe–O bonds, possibly involving oxyl radical character, relating to the catalytic activity.[24] A more recent Mössbauer spectroscopy study states the formation of Fe^{4+} in NiFe catalysts under catalytic potential.[22] It was proposed that Fe^{4+} sites are at edges or defects in the NiOOH structure and represent catalytically highly active sites; these active species itself remain invisible due to fast kinetic transformation coupled to O–O bond formation. The observed slow Fe^{4+} species were proposed to be present within the layers of a layered NiFe oxyhydroxide. Studies by Stevens[25] showed that Fe ions incorporated in the bulk of the oxide do not directly affect the catalytic activity, which mostly depends on incorporation of Fe to the edge of the layers. Scanning electrochemical microscopy experiments also showed evidence for surface kinetically slow and fast sites on mixed Ni–Fe oxides. According to Ahn *et al.*[26] the fast sites correspond to surface sites with higher Fe^{4+} content. Some recent computational DFT studies showed that charge transfer from Fe to Ni atoms in mixed nickel-iron oxides results in stabilization of Ni^{2+} and formation of Fe^{4+}. However, the stabilisation of Fe^{3+} may depend on its specific local environment.[27]

Based on the experimental evidence and computational experiments, the group of Bell has assigned the Fe^{3+} sites as the active sites for catalysis.[10] Görlin and coworkers[23] synthesized NiFe particles and activated them electrochemically. They also did not find evidence for Fe^{4+} and observed that Fe^{3+} can largely prevent the transition of Ni^{2+} to higher states.[23] They interpreted it as the consequence of a fast catalytic process which approaches the speed of the redox process of the Ni centers resulting in faster depletion of redox equivalents and consequently no accumulation of oxidized $Ni^{3+/4+}$ ions is observable. Regarding the role of the Fe^{3+} ion, we note that the mere presence of metal species in the +3 oxidation state (like Al^{3+}) does not result in enhanced catalytic activity.[28]

Nocera and coworkers suggested that the active site is located at the nickel atom and that Fe remains in +3 oxidation state, having a Lewis acid effect on the nickel atom promoting the formation of Ni^{4+}.[12] Formation of "active-oxygen" species at the nickel sites have been concluded from Raman experiments[29–31] and investigated O K-edge XAS[32] (for pure Ni oxides).

Another factor that adds complexity to the study of this type of catalysts is that different synthesis protocols are used, which normally lead to different and often also mixed phases.[10,13] Transformation to other phases under operation conditions can also be observed.[1,10] Moreover, the use of specific carbon substrates or carbon based supports also have been shown to improve the catalytic activity.[6,33,34]

Sometimes discussed as a charge transfer-effect[20] or a synergistic effect between metals,[35] the nature of the interaction between the Ni and Fe atoms within the catalyst material and specifically at the active site has remained unclear. More knowledge of the impact of the second metal in the dynamic processes during catalysis is needed for reaching a more complete understanding of the catalytic mechanism. In the present study, we approach the question of the role of the Fe sites by recently developed experimental technology, namely the combination of electrochemistry and X-ray absorption spectroscopy, including time-resolved *in situ* (or "operando") experiments in the millisecond domain.[36,37]

2. Experimental

2.1 Materials

Reagents: KOH (Sigma-Aldrich, ≥86%), $FeSO_4 \cdot 7H_2O$ (Sigma-Aldrich, ≥99%), $NiSO_4 \cdot 6H_2O$ (Riedel-deHaën, 99%), H_2SO_4 (Roth, 37%), KNO_3 (Roth, ≥99%). All reagents where used without further purification. Solutions were prepared with 18 MΩ cm^{-1} Milli-Q water.

2.2 Electrodeposition of the films

The electrodepositions were performed in a two-electrode system. Both electrodes were made of Toray Carbon Paper 120 (with 5 wt% PTFE wet proofing and 370 μm thickness, 590437-FuelCellStore) of 2 × 2 cm size. The backside of the electrodes was covered with Kapton tape (IM301202 polyimide film Goodfellow, 683-465-79), thereby supporting mechanical stability of the carbon electrode and preventing electrolyte leakage. The electrodes were placed parallel to each other with a separation of 0.5 cm and connected to a power supply (Thursby-Thandar PL330DP). All catalyst NiFe films of the present spectroscopic study were cathodically electrodeposited employing a constant current density of 250 mA cm^{-2} and a deposition period of 5 s, as described by Merrill and Dougherty.[38] The deposition solution consisted of 9 mM $NiSO_4$, 9 mM $FeSO_4$ and 25 mM $(NH_4)_2SO_4$ (pH of 2.5 adjusted with H_2SO_4). In the herein used catalyst films (deposited for 5 s) and in general for films cathodically electrodeposited for 1 to 20 s at a constant current of 250 mA cm^{-2}, the Ni : Fe concentration ratio consistently was close to 1.5 (Table S1†).

2.3 Electrochemical measurements

The NiFe catalyst was investigated at room temperature in 1 mol L^{-1} KOH solution using a single-compartment three-electrode electrochemical cell, a high surface area Pt mesh as a counter electrode, a hydrogen reference electrode (HydroFlex®, Gaskatel), and a potentiostat (SP-300, BioLogic Science Instruments). The solutions were neither stirred nor deaerated during experiments.

2.4 *In situ* X-ray absorption measurements

The X-ray measurements were performed at 20 °C at beamline KMC-3 (bending magnet) of the Berlin synchrotron radiation source (BESSY) operated by Helmholtz-Zentrum Berlin (HZB). A silicon (111) double-crystal monochromator selected the X-ray excitation energy. NiFe oxide deposited on Toray Carbon Paper 120, as described above, was mounted within a window of the *in situ* cell (three-electrode electrochemical cell with walls made from inert Teflon), which was filled with 1 M KOH and placed in the path of the X-ray beam, for back-side irradiation of the NiFe electrode (see Fig. S1,†ref. 36 and 37). The X-ray flux was comparably low (bending magnet beamline) and we used an out-of-focus geometry, to achieve an irradiated area on the

catalyst film of 11 × 3 mm. Thereby we could ensure that X-ray induced modifications of the sample were insignificant.

All X-ray absorption signals were collected in fluorescence mode, with detection at right angle to the exciting X-ray beam. The X-ray fluorescence passed a metal foil acting as a filter for suppression of scattered X-rays (10 μm thick Mn metal for measurements at Fe K-edge; 10 μm thick Co metal for measurements at Ni K-edge). The fluorescence was detected by a scintillation detector (19.6 cm^2 active area, 51BMI/2E1-YAP-Neg, Scionix; shielded by additional 2 μm Al filter against visible light) using a photomultiplier operated at 0.9 kV. The photomultiplier signal passed through a 1 MΩ resistor for current-to-voltage conversion to an amplifier (Stanford Research Systems, model SR560) with 6 dB per oct 10 Hz low-pass filtering and amplification of the signal by a factor of 20. With this 10 Hz low-pass filter, the rise time for a stepwise increase in input voltage was around 30 ms. The amplified signal was recorded with a sampling time of 10 ms by the analog-to-digital (AD) converter that is part of the used potentiostat (BioLogic SP300). The same potentiostat also operated the electrochemical cell and recorded (*via* a second AD converter) the signal from an ionization chamber monitoring the intensity of the incoming X-ray beam.

K-edge absorption spectra of the sample were recorded immediately before and after each time-resolved experiment, to normalize the time-resolved data and to assess film dissolution. Details about EXAFS simulations are provided in the ESI.†

3. Results and discussion

The cathodic deposition of transition metal catalyst represents an especially facile synthesis method and thus is of interest regarding technological application. A catalyst layer can be deposited quickly; its catalytic performance often is excellent.[38] A typical cyclic voltammetry (CV) of the here investigated NiFe oxyhydroxides is shown in Fig. 1.

To investigate the structural and redox dynamics of the NiFe catalyst, we performed X-ray absorption spectroscopy (XAS) *in situ* experiments, in combination with electrochemical protocols, *e.g.* cyclic voltammetry, as detailed in Experimental section and Fig. S1.† These experiments had been preceded by investigation of the experimental conditions that facilitate stable operation of the NiFe-based OER catalyst. Upon exposure of the cathodically electrodeposited catalyst films to oxidizing potential (1.50 V_{RHE}), pronounced changes in X-ray fluorescence intensities und spectra were observed for about 15 min (Fig. S3–S7†), but stable X-ray signals were obtained after conditioning at 1.50 V_{RHE} for 20 minutes. During the conditioning period, we observed a largely irreversible increase of the average Ni oxidation (by about +0.5, Fig. S4 and S5†) indicating that a significant fraction of the Ni ions became trapped in higher oxidations states. For ensuring stable operation conditions regarding catalyst dissolution and (slow) structural modification, all spectra and time courses reported in the following were recorded after conditioning at 1.50 V_{RHE} for 20 min. The 1.23 V_{RHE} spectra were collected after conditioning at 1.50 V_{RHE} followed by several minutes of equilibration at 1.23 V_{RHE}.

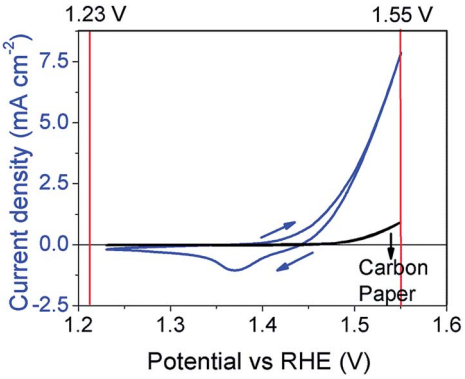

Fig. 1 Cyclic voltammogram (5 mV s^{-1}) of the NiFe catalysts electrodeposited on carbon paper (blue) and of the pure carbon paper support (black) in 1 M KOH. The CV features current peaks assignable to redox transitions of the catalyst material as well as a rise in current density above 1.45 V_{RHE} stemming from the catalytic water-oxidation current. The Ni : Fe stoichiometry of the catalyst material was around 1.5 (Table S1†). The two red lines show the potentials chosen to collect *in situ* X-ray spectra.

For the XANES spectra of the NiFe oxide collected at 1.23 and 1.55 V_{RHE}, we observed a shift in the Ni X-ray edge position by 1.1 eV (Fig. 2A). From measurements of Ni oxide references with known coordination environment and oxidation state (NiO, $Ni(H_2O)_6$, $LiNiO_2$, $K_2Ni(H_2IO_6)_2$),[11,23] we estimate that a change by one oxidation state unit is associated with a 1.6 eV shift in the edge position. Using this approximate calibration, we determine a change in Ni oxidation state from +1.9 (at 1.23 V_{RHE}) to +2.6 (at 1.55 V_{RHE}), that is, a transition from a Ni^{2+} to a Ni^{3+} material (this estimate was obtained without correction for the minor contribution of metallic Ni; see Fig. S9 and S10.† After correction for the metallic contribution, we obtain oxidation-state estimates of +2.0 and +2.9, respectively).

In previous Mössbauer spectroscopy experiments, it has been observed that about 20% of Fe^{3+} ions are converted to Fe^{4+} at potentials above 1.7 V_{RHE}.[22] This would result in an increase in the oxidation state from 3.0 to 3.2. In case of our X-ray absorption experiments at the Fe K-edge, we observed an almost negligible change in the edge position of about only 0.19 eV, for a potential increase from 1.23 V_{RHE} to 1.55 V_{RHE} (Fig. 2B). Based on comparison of reference iron compounds of known oxidation state (α-FeO(OH), α-Fe_2O_3, γ-Fe_2O_3, Fe_3O_4, FeO),[11,23] we estimate that an oxidation state change by one unit is associated with a shift of 5.1 eV in the edge position. Accordingly, about 4% of Fe atoms might shift its oxidation state from Fe^{3+} to Fe^{4+}. However, the analysis of such minor edge-shifts in terms of oxidation state changes is likely to be misleading whenever significant changes in the edge shape are present, as they are clearly visible in Fig. 2B. We propose that the slight change in the formally calculated edge position (using the "integral method"[39]) relates to a change in the shape of the spectra (visible at the primary absorption peak around 7131 eV) rather than being indicative of an oxidation state change of a minor fraction of Fe ions.

To corroborate the absence of major oxidation state changes of Fe ions, we also performed a series of X-ray edge

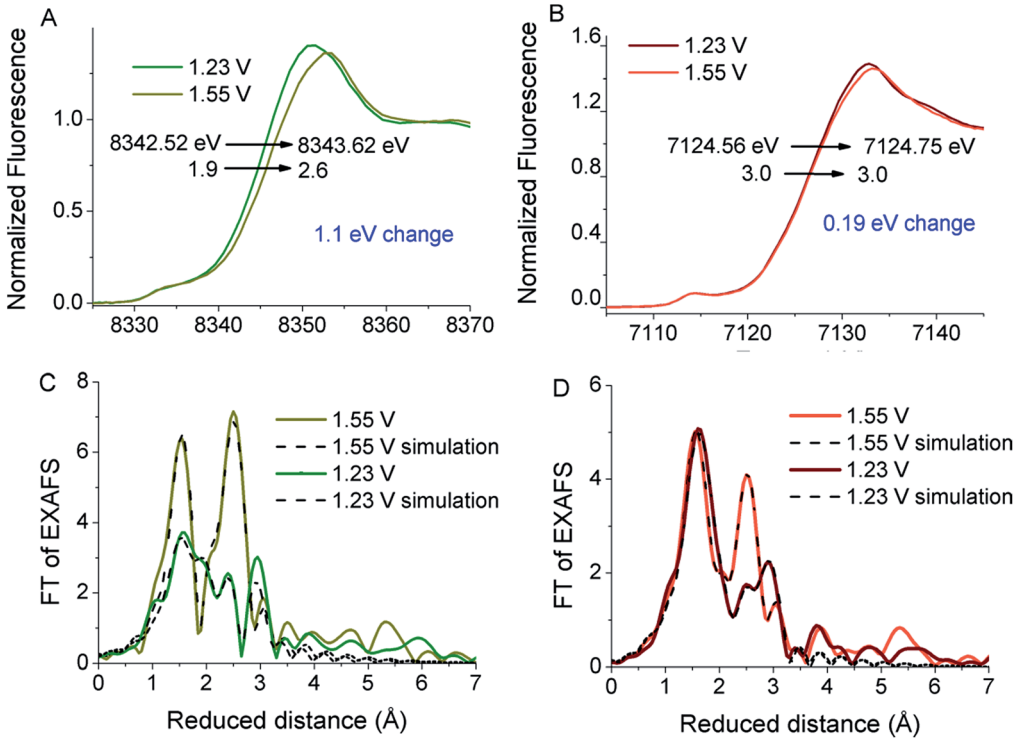

Fig. 2 *In situ* X-ray absorption spectroscopy in 1 M KOH for the NiFe catalyst electrodeposited on thin carbon paper. (A) Normalized Ni K-edge at 1.23 V_{RHE} and at 1.55 V_{RHE}. (B) Normalized Fe K-edge at 1.23 V_{RHE} and at 1.55 V_{RHE}. (C) Fourier-transformed EXAFS spectra at the Ni K-edge 1.23 V_{RHE} and at 1.55 V_{RHE} (lines) with the corresponding simulations (dotted lines). (D) Fourier-transformed EXAFS spectra at the Fe K-edge 1.23 V_{RHE} and at 1.55 V_{RHE} (lines) with the corresponding simulations (dotted lines) (a cosine window covering 10% of the left and right side of the *k*-range of the EXAFS spectra was used to suppress side lobes in the Fourier transforms). The simulation parameters are provided in Table 1 and the resulting EXAFS k^3 spectra are shown in Fig. S8.† In the case of panel C, a 10% metal contribution stemming from metallic nickel had been subtracted.

measurements with constant potential at the catalyst electrode ranging from 1.55 to 2.8 V_{RHE} (Fig. 3). The maximum oxidation state change observed from 1.23 V_{RHE} to the maximum potential 2.8 V_{RHE} in Fig. 3 might correspond to formation of about 8% of Fe^{4+} ions. However, even for highly positive potentials the shift of the Fe K-edge is small and likely explainable by changes in the shape of the X-ray edge resulting from changes in the Fe^{3+} coordination environment.

To study the structural changes caused by application of catalytic potentials, we performed *in situ* EXAFS experiments at the Ni and Fe K-edge after catalyst equilibration at 1.23 V_{RHE} and 1.55 V_{RHE}. The data with the corresponding simulations is shown in Fig. 2C and D; the parameters resulting from the simulations are shown in Table 1. The simulations were performed as a joint fit in which the bond lengths at both potentials are coupled to have the same value, and the Debye–Waller

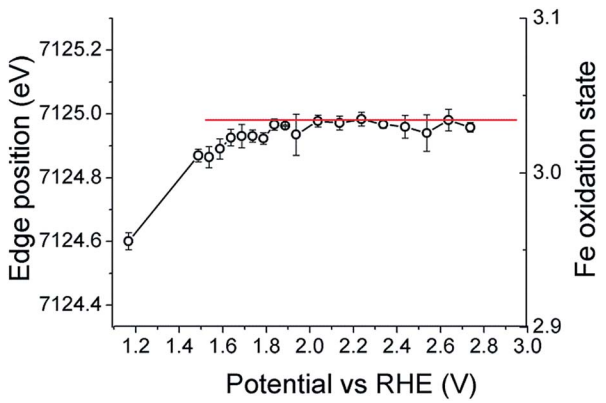

Fig. 3 Fe K-edge positions and formally estimated Fe oxidation states of the NiFe catalyst in 1 M KOH, as determined by *in situ* X-ray experiments. Each data point (and the indicated standard deviation) corresponds to the average of three measurements.

Table 1 EXAFS coordination numbers, *N*, as determined from EXAFS simulations[a]

	Distance[b] (in Å)	N^b 1.23 V	N^b 1.55 V
Ni–O_{short}	1.90(1)	1.9(3)	3.2(2)
Ni–O_{long}	2.06(1)	2.6(3)	0.9(4)
Ni–Ni_{metal}	2.49(1)	0.4(2)	0.5(1)
Ni–Ni_{short}	2.86(1)	1.2(4)	3.1(4)
Ni–Ni_{long}	3.07(1)	1.7(4)	1.4(4)
Fe–O_{short}	1.92(1)	2.5(3)	3.2(2)
Fe–O_{long}	2.05(1)	3.5(2)	2.4(3)
Fe–Fe_{metal}	2.52(1)	0.53(9)	0.58(9)
Fe–Ni_{short}	2.85(3)	0.2(7)	2(1)
Fe–Fe_{middle}	2.96(3)	2.0(3)	3.0(6)
Fe–Fe_{long}	3.12(2)	2.4(2)	2.1(4)

[a] σ = 0.063 Å, for all simulations. [b] The numbers in parenthesis correspond to the likely error in the last digit (1σ error range).

parameter is kept constant, to avoid over-parameterization. Using this simulation approach, EXAFS coordination numbers are obtained that represent the number of atom pairs at the respective distances for working potentials of 1.23 V_{RHE} and 1.55 V_{RHE}.

The simulations at the Ni K-edge show that two prominent atom pairs are detectable at 1.55 V_{RHE}: Ni–O pairs with R_{Ni-O} of 1.9 Å and Ni-metal pairs with R_{Ni-Me} of 2.87 Å. These distances are characteristic for a γ-NiOOH phase;[10] whereas the long Ni–O and Ni-metal distances of 2.06 and 3.07 Å prevailing at 1.23 V_{RHE} correspond to α-$Ni(OH)_2$ phase.[10] At 1.23 V_{RHE}, the two phases were detected roughly in a 1 : 1 ratio. At 1.55 V_{RHE}, the proportion of the γ-NiOOH phase was clearly increased.

In the simulations of the Fe edge EXAFS spectra, we observed an increase in the number of short Fe–O distances at 1.92 Å when increasing the potential from 1.23 V_{RHE} to 1.55 V_{RHE}. We also observed a pronounced increase in the EXAFS coordination number of Fe–metal distances at 2.85 Å. Formation of shorter distances is usually associated with an increase in oxidation state and deprotonation. In the case of iron, we did not observe indications of major Fe oxidation state changes in the edge spectra that could account for the pronounced structural changes detected in the EXAFS (Fig. 2D). The changes at the top of the Fe K-edge may be rather associated with formation of short Fe–O and Fe–metal distances detected by EXAFS analysis (Table 1). Bell and coworkers suggested that in a mixed Ni–Fe oxide phase, the structural changes are associated with an increase in the Ni oxidation state as well as shortening of metal–metal distances that affect the structure around the iron centers.[10] Our results support this hypothesis. These structural changes are fully reversible and are responsible for the changes at the top of the Fe edge in the XANES measurements (Fig. 2B and D).

To study electric-potential dependence and dynamics of the oxidation state changes, we performed cyclic voltammetry experiments combined with detection of X-ray fluorescence

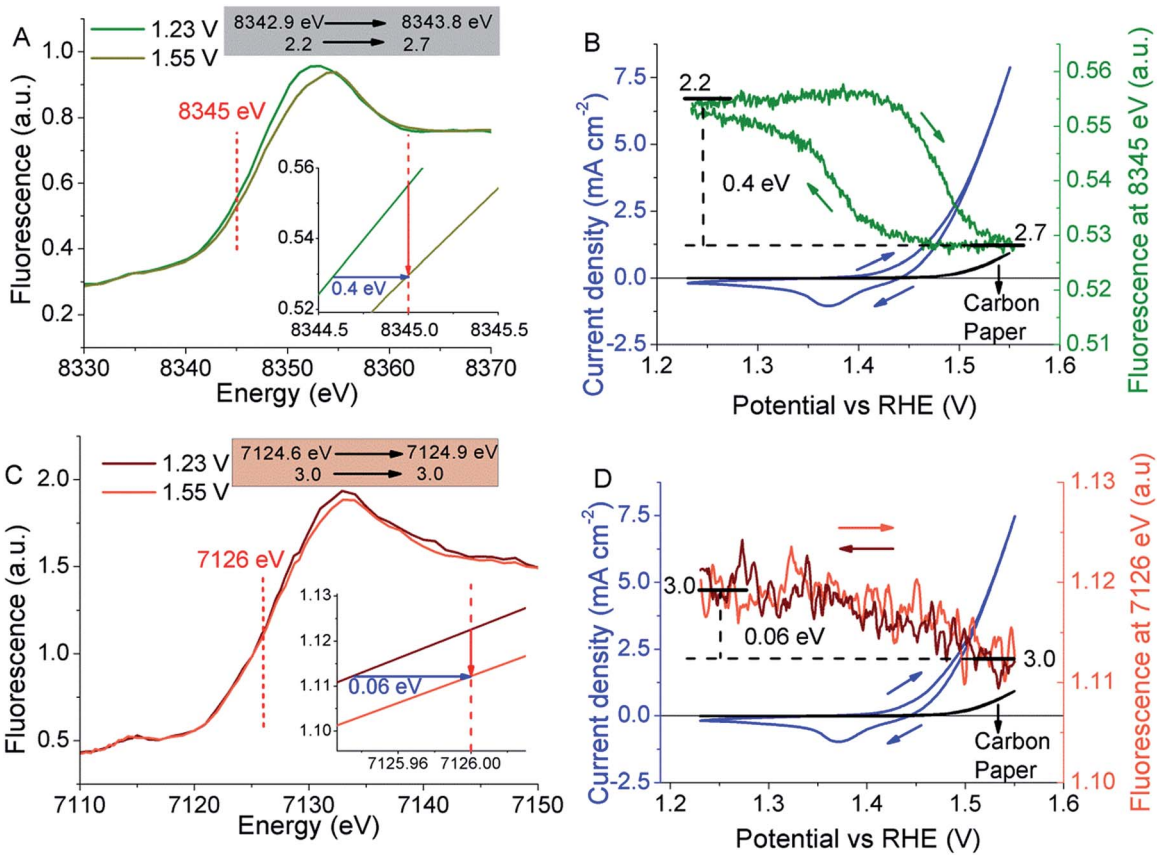

Fig. 4 *In situ* detection of X-ray absorption signal during a cyclic voltammogram (CV) (1 M KOH, NiFe catalyst sample deposited on carbon paper). (A) Non-normalized Ni K-edge spectra at 1.23 V_{RHE} and at 1.55 V_{RHE}. In the inset, the red arrow shows how the decrease in X-ray fluorescence is related to a shift in the edge position (blue arrow). The red dotted line represents the energy at which the X-ray beam was set (8345 eV). (B) *In situ* CV at the Ni Kedge (scan rate 5 mV s^{-1}, blue – current density on NiFe, grey – current density on carbon paper support, green – X-ray fluorescence at 8345 eV). Arrows indicate the scan direction. The decrease in the X-ray fluorescence is related to a shift of 0.4 eV in the edge position (7 measurements were averaged). (C) Non-normalized Fe K-edge spectra at 1.23 V_{RHE} and at 1.55 V_{RHE}. In the inset, the red arrow shows how the decrease in X-ray fluorescence is related to a shift in the edge position (blue arrow). The red dotted line represents the energy at which the X-ray beam was set (7126 eV). (D) *In situ* CV at the Fe K-edge (scan rate 5 mV s^{-1}, blue – current density on NiFe, grey – current density on carbon paper support, orange/dark red – X-ray fluorescence at 7126 eV). Arrows indicate the scan direction. The decrease in X-ray fluorescence is related to a shift of 0.06 eV in the edge position (7 measurements were averaged). The ohmic resistance of electrolyte and electrodes was 3 Ω; no *iR* drop correction was applied.

signals. In these experiments, we adjusted the X-ray energy at a position in the middle of the respective absorption edge (8345 eV for Ni, 7126 eV for Fe), and recorded the change in the X-ray K_α-fluorescence excited either at 8345 eV, for tracking oxidation state changes of Ni ions, or at 7126 eV, for tracking oxidation state changes of Fe ions. The rational of these experiments is illustrated by Fig. 4A and C, where the X-ray edge spectra of the NiFe catalyst are shown for short-term equilibration at 1.23 V_{RHE} and 1.55 V_{RHE}. We detect a shift of Ni K-edge position by 0.4 eV assignable to Ni oxidation from about +2.2 to +2.7. This oxidation state change and the parallel energy shift of the X-ray edge position correspond to a decrease of the X-ray fluorescence intensity when measured at a suitably selected excitation energy of, *e.g.* 8345 eV, meaning that any increase in the oxidation state is reflected as a decrease in the X-ray fluorescence and *vice versa*.

The dynamics of the X-ray fluorescence intensity during a CV are shown in Fig. 4B. We can observe that parallel to the oxidation wave appearing in the CV, the X-ray fluorescence decreases, and it again increases to the same level as the film is reduced in the backward scan. The corresponding X-ray edge shifts (quantified with "integral method" of ref. 39) and estimated changes in the Ni oxidation state are shown as insets in Fig. 4A. We conclude that the Ni oxidation state changes cover a range from about +2.2 to +2.7 (we note that the oxidation state change suggested by the data of Fig. 4 is smaller than in the data of Fig. 2A, 0.5 *vs.* 0.7, likely because of dissimilar levels of equilibration at 1.23 V_{RHE} resulting in different levels of Ni ions trapped in higher oxidation states).

At the Fe K-edge, the X-ray signal suggests that there are only insignificant potential-dependent changes in the Fe oxidation state (Fig. 4D) (on a first glance, the X-ray fluorescence collected the Fe edge during a CV appears as being especially noisy, but this mostly results from an expanded *y*-axis scaling used in Fig. 5D). There might be a small shift in the X-ray edge position of 0.06 eV, but the changes in the X-ray intensity are too close to the noise level for any reliable quantitative estimate. Thus we conclude that the X-ray fluorescence detected during a CV does not support oxidation state changes of the Fe ions, which is in line with the XANES data collected after equilibration at selected potentials (Fig. 2B and 3).

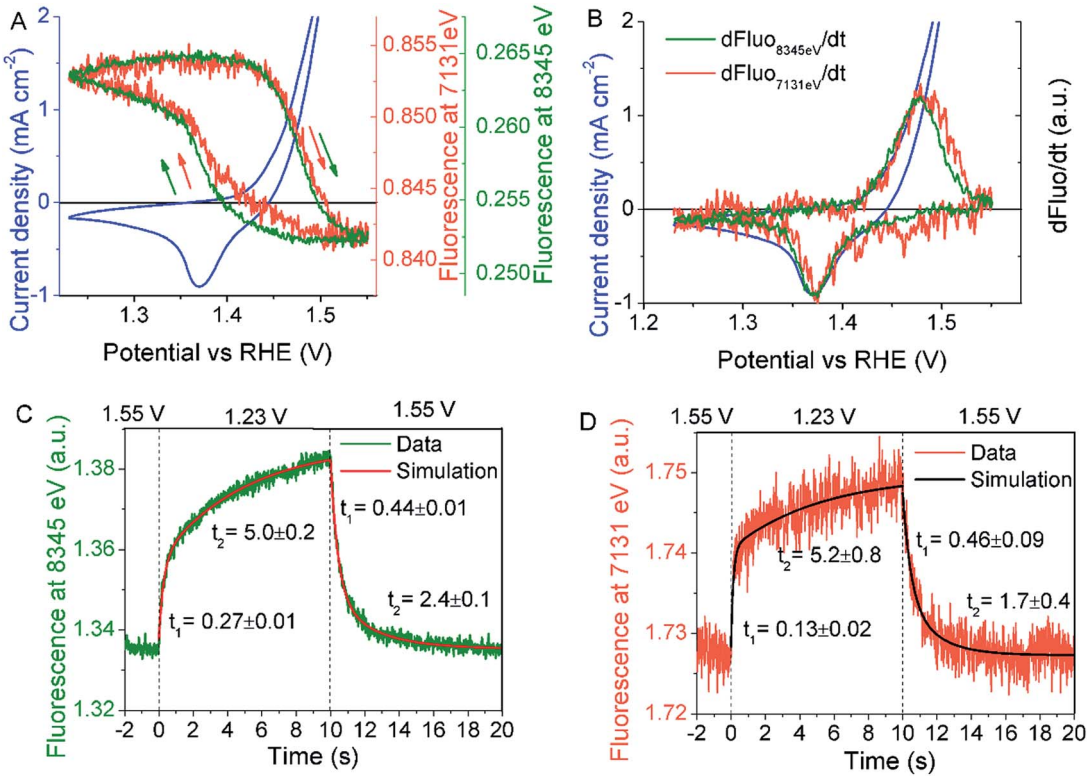

Fig. 5 Time-resolved detection of the X-ray fluorescence signal during a cyclic voltammogram (CV, in (A) and (B)) and after a step-wise change of the electrode potential (C and D) of the NiFe catalysts deposited on carbon paper in 1 M KOH. (A) *In situ* collection of X-ray data in parallel to recording a CV with 5 mV s^{-1}. Blue – current density, red – X-ray fluorescence at 7131 eV (absorption maximum of the Fe K-edge), green – X-ray fluorescence at 8345 eV (center of the edge rise of the Ni K-edge). (B) Derivative (with respect to time) of the X-ray absorption signal ($dF_{X\text{-}ray}/dt$), for direct comparison with current densities (color code as in (A)). The panels (C) and (D) show *in situ* time courses obtained for sudden, step-wise changes of the electric potential (90 potential steps from 1.23 to 1.55 V_{RHE} and back to 1.23 V_{RHE} are averaged) at (C) the Ni K-edge (8345 eV), and at (D) the Fe K-edge (7131 eV). The data was simulated (least-square curve fitting) using a sum of two exponential functions; the simulation parameters are provided in Table S2.† An alternative simulation of the data in (D) with time constants of 0.27 ms and 5.0 ms in the reducing transition resulted in equally good match of data and simulated curve (Table S3†). For presentation of (C) and (D) with expanded time scale, see Fig. S11 and S12.† The ohmic resistance was 3 Ω; no *IR*-drop correction was applied.

We also tracked the X-ray signal during a CV for excitation at an X-ray energy at the absorption maximum of the Fe K-edge (7131 eV). Thereby a very similar plot as the one for the oxidation state changes at the Ni-edge is obtained (Fig. 5A). The potential-dependent changes of the X-ray fluorescence for excitation at 7131 eV likely reflects modification of the coordination environment of Fe ions that occur concomitantly with oxidation of the Ni ions. Comparison to the EXAFS data of Fig. 2 and Table 1 suggests that the structural changes involve the formation of short Fe–O distances of 1.92 Å and short Fe–Ni distances of 2.85 Å.

The X-ray signals reflect the Ni oxidation state, for excitation at the Ni K-edge at 8345 eV, and structural changes at the Fe K-edge, for excitation at the Fe K-edge at 7131 eV. If the derivative of these two X-ray signals are scaled to the current of the CV, their electric-potential dependencies match very closely the current of the reductive CV wave. The close match of the derivative of the Ni signal (8345 eV), which reflects changes in the Ni oxidation state, and the current density suggests that the current wave is assignable to oxidation of Ni ions.

The close match of the CV current with the structural X-ray signal detected at the Fe K-edge at 7131 eV implies that the Ni oxidation state changes are "sensed" by iron ions resulting in a modification of their coordination environment. There are no indications for a redox-wave that is not accounted for by the X-ray signals. Consequently, the herein reported data does not provide evidence for formation of oxidized oxygen species. However, we cannot exclude further redox processes occurring simultaneously (at the same potentials) with the dominating Ni oxidation.

To study timescale and sequence of the events, we performed experiments in which the energy of the incident beam had been set (i) at the center of the Ni edge (8345 eV) and (ii) at the top of the Fe edge (7131 eV). The potential was switched from 1.55 V_{RHE} to 1.23 V_{RHE} with steps of 10 s duration at 1.55 V_{RHE}. The potential step protocol was repeated 90 times for improving the signal-to-noise ratio by signal averaging. We find that the time courses reflecting Ni oxidation/reduction (at 8345 eV, Fig. 5C) and the time courses likely reflecting shortening/lengthening of Fe–ligand distances (at 7131 eV, Fig. 5D) are similar. For quantitative analysis, the time courses were simulated bi-exponentially according to:

$$F = A + Be^{\frac{-t}{t_1}} + Ce^{\frac{-t}{t_2}} \quad (1)$$

where the time constants correspond to reciprocal rate constants ($k_i = 1/t_i$). Thereby we find that the time courses of the X-ray signals of Fig. 5C and D both exhibit a fast phase with time constants in the reductive and oxidative transition around 250 ms and 450 ms, respectively. The clearly slower phase was characterized by time constants of about 5 s (reductive transition) and 2 s (oxidative transition). These similarities suggest that the Ni oxidation state change detected at 8345 eV and structural change in the Fe ligand environment detected at 7131 eV occur simultaneously, fully in line with the analysis of the X-ray signals collected during a CV. There also was no sigmoidal rise or lag phase behaviour detectable that would indicate sequential reactions (Fig. S11 and S12†). In summary, the time-resolved X-ray data excludes that the changes in the Fe ligand environment occur before or after the Ni redox reaction, but indicates that these are simultaneously occurring, directly coupled processes. At present, it remains unexplained why the redox transitions proceed with pronouncedly biphasic reaction kinetics. This aspect requires further investigation but is beyond the scope of our current study.

4. Conclusions

Comparison of the *in situ* XANES and EXAFS collected after equilibration at non-catalytic potential (1.23 V_{RHE}) and catalytic potential (1.55 V_{RHE}) suggests structural modifications that likely are related to the $Ni^{2+/3+}$ redox transition of the oxyhydroxide material at about 1.43 V_{RHE}. These structural modifications involve a transition from motifs prevalent in layered double-hydroxide, $M(\mu_3\text{-}OH)_2$, to motifs found in layered oxyhydroxides, $M(\mu\text{-}O)(\mu_3\text{-}OH)$, or layered dioxides, $M(\mu_3\text{-}O)_2$. Whereas the Ni oxidation state change is unambiguously detectable, the XANES spectra do not provide evidence for involvement of an $Fe^{3+/4+}$ redox transition. However, comparison of the EXAFS spectra collected at non-catalytic and more oxidizing, catalytic potential reveals for Ni and Fe similar modifications of the first coordination sphere (shorter M–O distances in the oxidized state) and in the second coordination sphere (shorter M–M distances in the oxidized state).

A shortening of M–O distances typically is indicative of an increased metal oxidation state, because metal oxidation often induces strengthening (contraction) of the M–O bond. Therefore, the observed shortening of Fe–O distances might indicate $Fe^{3+/4+}$ oxidation in a significant fraction of Fe sites. The changes in the Fe–M distance follow the modifications observed in Ni–M distances, namely formation of short M–M distances of about 2.86 Å in the oxidized state of the catalyst. This observation suggests that, at least in the oxidized state at catalytic potential, a major fraction of the Fe ions is part of the oxyhydroxide lattice with geometrical parameters characteristic of a pure $NiO(OH)_x$. Therefore, the short Fe–O distances could result from "enslavement" of the Fe coordination environment by changes in the oxyhydroxide lattice, which are caused by oxidation of the Ni ions. In conclusion, the transition to the oxidized, catalytically active state may involve either (i) an atypical $Fe^{3+/4+}$ redox transition or (ii) a modification of the Fe coordination environment that is enforced by the change in the lattice geometry caused by $Ni^{2+/3+}$ oxidation.

The XAS results reported here are qualitatively well in line with previous reports for various NiFe-based OER catalyst. However, the extent of Ni oxidation state changes and the number of Fe ions within the layered oxyhydroxides differ between NiFe catalysts obtained by different synthesis routes, for reasons that remain inadequately understood. We note that the present results indicate that neither all Ni nor all Fe ions participated in the discussed redox transition.

For additional insight, we combined electrochemistry with time-resolved detection of the X-ray fluorescence excited at selected X-ray energies. In the CV experiment, the current waves

assignable to redox-state changes of the catalyst material match precisely the X-ray signal that tracks the $Ni^{2+/3+}$ oxidation state changes. From the absence of discrepancies, we conclude that sizeable redox currents are exclusively associated with redox transition that involve oxidation/reduction of Ni ions. All further modifications of the electronic or atomic structure are likely coupled to the Ni oxidation state change. This conclusion is confirmed by tracking the X-ray signal reflecting changes in the Fe ligand environment. These structural changes occur concomitantly to the $Ni^{2+/3+}$ oxidation state change. There is no indication of a separate $Fe^{3+/4+}$ redox transition at a distinctively different potential. Similarly, the responses to potential steps reveal simultaneous changes in Ni oxidation state and modification of the Fe coordination environment. Within the time-resolution of the experiment, we cannot detect any indications for a preceding reaction step.

Our finding that modification of the Fe coordination environment proceeds simultaneously with the $Ni^{2+/3+}$ redox reaction—at the same redox potentials and with the same temporal kinetics—is well in line with the second option discussed above: changes in the Fe coordination environment are enforced by a Ni-dominated lattice geometry. However, neither Fe^{4+} nor $Fe^{3+}O^{\bullet}$ formation directly coupled to Ni oxidation can be fully ruled out. We also emphasize that redox reactions involving only a minority of metal ions or ligand sites could remain invisible in the herein reported experiments. Similarly, redox intermediates would remain invisible if they were only transiently formed, *e.g.* the recently reported Fe^{6+} sites in NiFe oxyhydroxides.[40]

Conflicts of interest

There are no conflicts to declare.

Acknowledgements

We gratefully acknowledge financial support by the Bundesministerium für Bildung und Forschung (IN-SITU-XAS, 05K16KE2; CO2EKAT, 03SF0523B) and the Deutsche Forschungsgemeinschaft (Priority Program SPP 1613, DA 402/7-2; Cluster of Excellence UniCat, EXC 314-2). D. G.-F. thanks Prof. Roberto Urcuyo (San José, Costa Rica) for fruitful discussion and his generous support that facilitated completion of this study. We thank Dr Mikaela Görlin (TU Berlin, now Stockholm University) for sharing her expertise in numerous discussions on NiFe oxyhydroxides. We acknowledge the Helmholtz-Zentrum Berlin (HZB) for providing access to the beamline KMC-3 at the Berlin synchrotron radiation source (BESSY, Berlin-Adlershof) and we thank the BESSY/HZB staff members, in particular Dr Ivo Zizak, for important support.

References

1 L. Trotochaud, J. K. Ranney, K. N. Williams and S. W. Boettcher, *J. Am. Chem. Soc.*, 2012, **134**, 17253–17261.
2 M. Gong and H. Dai, *Nano Res.*, 2014, **8**, 23–39.
3 F. Song and X. Hu, *Nat. Commun.*, 2014, **5**, 1–9.
4 J. R. Swierk, S. Klaus, L. Trotochaud, A. T. Bell and T. D. Tilley, *J. Phys. Chem. C*, 2015, **119**, 19022–19029.
5 X. Lu and C. Zhao, *Nat. Commun.*, 2015, **6**, 1–7.
6 W. Ma, R. Ma, C. Wang, J. Liang, X. Liu, K. Zhou and T. Sasaki, *ACS Nano*, 2015, **9**, 1977–1984.
7 R. L. Tichenor, *Ind. Eng. Chem.*, 1952, 973–977.
8 G. Młynarek, M. Paszkiewicz and A. Radniecka, *J. Appl. Electrochem.*, 1984, **14**, 145–149.
9 D. A. Corrigan, *J. Electrochem. Soc.*, 1987, **134**, 377.
10 D. Friebel, M. W. Louie, M. Bajdich, K. E. Sanwald, Y. Cai, A. M. Wise, M. J. Cheng, D. Sokaras, T. C. Weng, R. Alonso-Mori, R. C. Davis, J. R. Bargar, J. K. Nørskov, A. Nilsson and A. T. Bell, *J. Am. Chem. Soc.*, 2015, **137**, 1305–1313.
11 M. Görlin, J. F. De Araujo, H. Schmies, D. Bernsmeier, S. Dresp, M. Gliech, Z. Jusys, P. Chernev, R. Kraehnert, H. Dau and P. Strasser, *J. Am. Chem. Soc.*, 2017, **139**, 2070–2082.
12 N. Li, D. K. Bediako, R. G. Hadt, D. Hayes, T. J. Kempa, F. von Cube, D. C. Bell, L. X. Chen and D. G. Nocera, *Proc. Natl. Acad. Sci.*, 2017, **114**, 1486–1491.
13 J. Landon, E. Demeter, N. Inoğlu, C. Keturakis, I. E. Wachs, R. Vasić, A. I. Frenkel and J. R. Kitchin, *ACS Catal.*, 2012, **2**, 1793–1801.
14 M. W. Louie and A. T. Bell, *J. Am. Chem. Soc.*, 2013, **135**, 12329–12337.
15 D. K. Bediako, B. Lassalle-Kaiser, Y. Surendranath, J. Yano, V. K. Yachandra and D. G. Nocera, *J. Am. Chem. Soc.*, 2012, **134**, 6801–6809.
16 P. W. T. Lu and S. Srinivasan, *J. Electrochem. Soc.*, 1978, **125**, 1416.
17 L. Trotochaud, S. L. Young, J. K. Ranney and S. W. Boettcher, *J. Am. Chem. Soc.*, 2014, **136**, 6744–6753.
18 A. M. Smith, L. Trotochaud, M. S. Burke and S. W. Boettcher, *Chem. Commun.*, 2015, **51**, 5261–5263.
19 H. Bode, K. Dehmelt and J. Witte, *Electrochim. Acta*, 1966, **11**, 1079–1087.
20 M. K. Bates, Q. Jia, H. Doan, W. Liang and S. Mukerjee, *ACS Catal.*, 2016, **6**, 155–161.
21 S. Klaus, Y. Cai, M. W. Louie, L. Trotochaud and A. T. Bell, *J. Phys. Chem. C*, 2015, **119**, 7243–7254.
22 J. Y. C. Chen, L. Dang, H. Liang, W. Bi, J. B. Gerken, S. Jin, E. E. Alp and S. S. Stahl, *J. Am. Chem. Soc.*, 2015, **137**, 15090–15093.
23 M. Görlin, P. Chernev, J. F. De Araújo, T. Reier, S. Dresp, B. Paul, R. Krähnert, H. Dau and P. Strasser, *J. Am. Chem. Soc.*, 2016, **138**, 5603–5614.
24 M. Balasubramanian, C. a. Melendres and S. Mini, *J. Phys. Chem. B*, 2000, **104**, 4300–4306.
25 M. B. Stevens, C. D. M. Trang, L. J. Enman, J. Deng and S. W. Boettcher, *J. Am. Chem. Soc.*, 2017, **139**, 11361–11364.
26 H. S. Ahn and A. J. Bard, *J. Am. Chem. Soc.*, 2016, **138**, 313–318.
27 J. C. Conesa, *J. Phys. Chem. C*, 2016, **120**, 18999–19010.
28 Y. Vlamidis, E. Scavetta, M. Gazzano and D. Tonelli, *Electrochim. Acta*, 2016, **188**, 653–660.

29 B. J. Trześniewski, O. Diaz-Morales, D. A. Vermaas, A. Longo, W. Bras, M. T. M. Koper and W. A. Smith, *J. Am. Chem. Soc.*, 2015, **137**, 15112–15121.
30 M. Merrill, M. Worsley, A. Wittstock, J. Biener and M. Stadermann, *J. Electroanal. Chem.*, 2014, **717–718**, 177–188.
31 O. Diaz-Morales, D. Ferrus-Suspedra and M. T. M. Koper, *Chem. Sci.*, 2016, **7**, 2639–2645.
32 M. Yoshida, Y. Mitsutomi, T. Mineo, M. Nagasaka, H. Yuzawa, N. Kosugi and H. Kondoh, *J. Phys. Chem. C*, 2015, **119**, 19279–19286.
33 M. Gong, Y. Li, H. Wang, Y. Liang, J. Z. Wu, J. Zhou, J. Wang, T. Regier, F. Wei and H. Dai, *J. Am. Chem. Soc.*, 2013, **135**, 8452–8455.
34 Y. Qiu, L. Xin and W. Li, *Langmuir*, 2014, **30**, 7893–7901.
35 F. Yang, K. Sliozberg, I. Sinev, H. Antoni, A. Bähr, K. Ollegott, W. Xia, J. Masa, W. Grünert, B. R. Cuenya, W. Schuhmann and M. Muhler, *ChemSusChem*, 2017, **10**, 156–165.
36 I. Zaharieva, D. González-Flores, B. Asfari, C. Pasquini, M. R. Mohammadi, K. Klingan, I. Zizak, S. Loos, P. Chernev and H. Dau, *Energy Environ. Sci.*, 2016, **9**, 2433–2443.
37 R. D. L. Smith, C. Pasquini, S. Loos, P. Chernev, K. Klingan, P. Kubella, M. R. Mohammadi, D. Gonzalez-Flores and H. Dau, *Nat. Commun.*, 2017, **8**, 2022.
38 M. Merrill and R. Dougherty, *J. Phys. Chem. C*, 2008, **112**, 3655–3666.
39 H. Dau, P. Liebisch and M. Haumann, *Anal. Bioanal. Chem.*, 2003, **376**, 562–583.
40 B. M. Hunter, N. B. Thompson, A. M. Muller, G. R. Rossman, M. G. Hill, J. R. Winkler and H. B. Gray, *Joule*, 2018, **2**, 1–17.